The Influence of Wave Characteristics, Tides, and Installation Conditions of L-Shaped OWC Wave Energy Converter on Energy Absorption Capability

Adnan Sandy Dwi Marta
Research Center for Hydrodynamics Technology, National Research and Innovation Agency, BRIN

Deendarlianto
Department of Mechanical and Industrial Engineering, Faculty of Engineering, Universitas Gadjah Mada

Kongko, Widjo
Research Center for Hydrodynamics Technology, National Research and Innovation Agency, BRIN

Aprijanto
Research Center for Hydrodynamics Technology, National Research and Innovation Agency, BRIN

他

https://doi.org/10.5109/7236900

出版情報：Evergreen. 11 (3), pp.2607-2617, 2024-09. 九州大学グリーンテクノロジー研究教育センター
バージョン：

The Influence of Wave Characteristics, Tides, and Installation Conditions of L-Shaped OWC Wave Energy Converter on Energy Absorption Capability

Adnan Sandy Dwi Marta[1,2,*], Deendarlianto[2,*], Widjo Kongko[1], Aprijanto[1], Ahmad Taufiqur Rohman[3], Agus Wibowo[4], Irfan Yahya Ikhsanudin[4]

[1]Research Center for Hydrodynamics Technology, National Research and Innovation Agency, BRIN, Surabaya, 60112, Indonesia

[2]Department of Mechanical and Industrial Engineering, Faculty of Engineering, Universitas Gadjah Mada, Jl. Grafika No. 2, Yogyakarta, 55281, Indonesia

[3]Research Center for Energy Conversion and Conservation, National Research and Innovation Agency, BRIN, Tangerang Selatan, 15413, Indonesia

[4]Directorate of Laboratory Management, Research Facilities, and Science and Technology Park, National Research and Innovation Agency, BRIN, Tangerang, 15314, Indonesia

*Author to whom correspondence should be addressed:
E-mail: adna001@brin.go.id; deendarlianto@ugm.ac.id

(Received May 11, 2024: Revised June 29, 2024: Accepted August 2, 2024).

Abstract: The investigation with a numerical study examines how water conditions, including wave height and period, tidal variations, and the depth of the L-OWC device, impact wave energy generation. Utilizing the Reynolds-Averaged Navier-Stokes equations and the RNG turbulence model, the second-order Stokes wave motion is simulated. The Volume of Fluid (VOF) method with two fluids captures the free surface elevation. The purpose of this study is to investigate how various wave condition parameters, tidal effects, and water depth conditions of an L-OWC device can effect water oscillations within the chamber, airflow velocity in the turbine duct, and the differential pressure in the L-OWC device chamber. Findings highlight the significant influence of wave characteristics, tides, and deployment depth on L-OWC performance. The heightened water surface oscillation in the L-OWC chamber has led to higher air flow velocity and differential pressure, resulting in increased power. Optimal performance was observed with longer wave periods, notably under High Water Levell (HWL) and the water depth at the device installation is 0.85 cm (D085) conditions, yielding 337 watts of power output, in tests at a laboratory scale of 1:10.

Keywords: Oscillating Water Column; L-OWC; waters characteristics; installation conditions; tidal variations; OWC; performance.

1. Introduction

The utilization of ocean waves as a renewable energy source holds significant promise, offering a substantial contribution to electricity generation, particularly for coastal regions[1)2)]. Wave energy, if harnessed comprehensively, has the potential to supply roughly twice the current global annual energy consumption[3)]. Notably, its consistent energy provision sets it apart from other renewable sources, providing a more reliably predictable energy delivery schedule[4)]. Worldwide research has been done on the Oscillating Water Column (OWC), a wave energy converters (WEC) device. This device features a steel or concrete container that is partially immersed in the sea and open at the bottom[5)].

The Oscillating Water Column (OWC) is made up of an air turbine and an open area that extends below the surface to the sea. Optimizing the performance of the OWC device is mostly dependent on the design of the turbine and the chamber[6)]. An OWC plant's overall efficiency is influenced by both the air turbine-based secondary conversion phase and the air chamber-based primary conversion phase[7)]. A lot of recent research has been done on OWC converter geometry. One specific design involves an OWC variant with an additional front wall, connecting the chamber to the sea through a vertical channel[8)]. This change raises the water column's intrinsic oscillation frequency, which leads to the equipment being categorized as the U-shaped Oscillating Water Column (OWC).[9]. To increase the resonance frequency of the system, another design called the L-shaped OWC has a channel orientated in the direction of wave propagation[10]. In the case of an L-shaped OWC with a relatively short entrance channel compared to the chamber's length, there is an observed increase in the average power output in long waves[11].

The initial theoretical investigation of the air chamber and turbine combination is predicated on the idea that the turbine's pressure differential and relative flow rate have a straightforward relationship that can be either linear or square[12,13]. In recent years, the predominant emphasis in Oscillating Water Column (OWC) study has been on wells turbine, impulses, including radial[14], axial[15] and more recently, biradial designs[16]. In terms of the chamber, its geometry must be tailored to the characteristics of the waves entering it in order to maintain the water column oscillation in resonant or near-resonant states for prolonged periods of time[17,18].

Research has been conducted on an L-shaped chamber OWC with relatively long wave period characteristics, specifically ranging from 3.18s to 6.7s. The optimal power occurs when the wave height is 0.25m, happening at a period of 3.18s, and decreases as the period lengthens, reaching 206 Watts[5]. Full-scale implementation was conducted by Wave Swell Energy at the King Island Project with an L-shaped OWC equipped with pontoons featuring an output specification of 200 kW. Scaling the device down to 1:8, it matches wave characteristics for wave periods ranging from 3.18s to 6.72s and wave heights ranging from 0.0625m to 0.25m, with a power output of 138 Watts[19].

The objectives of this research is to investigate how different wave condition parameters, tidal effects, and water depth conditions on the L-OWC device can impact the pressure differential between the L-OWC chamber and turbine duct, the air flow velocity in the turbine duct, and the water oscillation inside the chamber, all of which can have an impact on the wave energy converter device's power output. The increased oscillation of the water surface in the L-OWC chamber leads to higher air flow velocity and differential pressure, resulting in increased power output. The optimal performance in this experiment was achieved with relatively long wave periods, particularly under High Water Level (HWL) conditions and when the water depth for device installation was at its deepest. This produced the most optimal power output among other test scenarios, in a 1:10 scale laboratory test. This study is motivated by a pre-feasibility study for a wave power plant in Maluku, Indonesia, characterized by short wave periods and relatively high tidal levels. The reference design for this study is the L-OWC, which has been successfully commissioned in Australia by Wave Swell Energy[20]. This research highlights the importance of selecting a chamber design that matches the wave characteristics when installing a wave power plant.

2. Numerical Methods

2.1 Governing equations

The research methodology employed involves numerical simulations using governing equations and parameters that have been validated through experimental data.The computational tool employed for the numerical simulations in this study is Flow-3D™ version 11, a Computational Fluid Dynamics (CFD) software. The Navier-Stokes and continuity equations are among the governing equations that describe the behavior of an incompressible Newtonian fluid. These equations are represented as follows in vector notation[21][22]:

$$\rho\left(\frac{\partial v}{\partial t} + v.\nabla v\right) = \nabla \mathrm{P} + \mu\nabla^2 v + \rho \mathrm{g} \qquad (2.1)$$

$$\nabla . v = 0 \qquad (2.2)$$

where ρ represents the fluid density, P denotes pressure, v stands for velocity, μ is the dynamic viscosity, ∇^2 signifies the vector Laplacian, g represents the acceleration due to gravity, t denotes time, and g denotes the acceleration due to gravity.

Like the classical k-ε turbulent model, The main purpose of the RNG turbulence model is to calculate average turbulence-related parameters, like turbulent energy and dissipation rate[23]. But the constants used in the k-ε model are derived from experimental evidence, whereas the RNG model's constants are found through theoretical derivations. In regions with low-intensity turbulence and shear fluid, FLOW-3D™ prefers the RNG model over the k-ε model because it can yield more accurate results[23]. To precisely represent and manage turbulent effects, the k-ε renormalization group (RNG) turbulence model is also utilized[24]. The k -ε RNG model's governing equations are written as follows[25]:

$$\frac{\partial(\rho k)}{\partial t} + \frac{\partial(\rho k u_i)}{\partial x_i} = \frac{\partial}{\partial x_j}\left[\left(\mu + \frac{\mu_t}{\sigma_k}\right)\frac{\partial k}{\partial x_j}\right] + P_k - \rho\epsilon \qquad (2.3)$$

$$\frac{\partial(\rho\epsilon)}{\partial t} + \frac{\partial(\rho\epsilon u_i)}{\partial x_i} = \frac{\partial}{\partial x_j}\left[\left(\mu + \frac{\mu_t}{\sigma_\epsilon}\right)\frac{\partial k}{\partial x_j}\right] + C_{1\epsilon}\frac{\epsilon}{k}P_k - C_{2\epsilon}^{*}\rho\frac{\epsilon^2}{k} \qquad (2.4)$$

Density and viscosity in the interface grids, for example, can be calculated using the volume fraction of the two phases and utilized in the momentum equation[26]. The density and viscosity equations corresponding to the free surface grids are provided by:

$$\rho = f_0\,\rho_0 + f_1\,\rho_1 \qquad (2.5)$$

$$v = f_0\,v_0 + f_1\,v_1 \qquad (2.6)$$

The fluid density is denoted by ρ, the kinematic viscosity by ν, and the volume fraction by f in this instance. In addition, air is represented by the subscript 1 and water by the subscript 0.

In this numerical simulation of the OWC, two fluids, water, and air are incorporated. To analyze the OWC, the Volume of Fluid method (VOF) is used, which involves two different fluids[27,28]. The free surface elevation is tracked and the air-water contact is predicted using the VOF approach[29]. he following is the expression of the equation controlling the volume fraction:

$$\frac{\partial f_m}{\partial t} + \nabla.(f_m.U) = 0 \qquad (2.7)$$

Where f_m is the volume fraction constrained by $0 \leq f_m \leq 1$; $f_m = 1$ indicates that the grid is fully occupied by mth fluid, $f_m = 0$ indicates that no m^{th} fluid exists in the grid, and $0 < f_m < 1$ implies the existence of an interface between water and air fluids. where U represents the velocity field [23].

FLOW-3D™ integrates a sophisticated advection algorithm that makes use of an upwind-difference approach of second order that maintains monotonicity[30]. Utilizing this monotonicity-preserving method, one may estimate the advection of many properties in FLOW-3D™, such as momentum, density, energy, and fluid percentage. By using second-order polynomial estimates for the advected quantity in each coordinate direction, the higher-order discretization method is accomplished[31]. The computed value of the flux through a cell-face, designated as Q*, for a variable Q being advanced in the x-direction is ascertained as follows:

$$Q^* = Q_i + \frac{1}{2}A(1 - C)\delta x_i \qquad (2.8)$$

Where δx_i is the cell size, C is the Courant number, Q_i is the cell-centered value, $\frac{u\,.\,\delta t}{\delta x_i}$. A is an approximation of the first derivative of Q at position $x_0 \frac{1}{6}\,(1 - 2C)\,\delta x_i$ inside the cell, and it is second-order.

2.2 Computational fluid domain

Using Cartesian coordinates, the simulation domain is divided into cubic or quadrilateral mesh elements using the technique known as Cartesian meshing. In this method, a square-based grid is created inside the simulation domain[32]. Mesh impact on geometry is assessed using the Fractional Area Volume Obstacle Representation (FAVOR) technique[31].

Figure 1 illustrates the four essential conditions constituting the boundary conditions for this research. The 2D wave flume length of the CFD complies with HYDRALAB guidelines[33]. The simulation's wall widths are adjusted to correspond with the test model's width. The upstream inlet conditions are varied based on the wave height and period, represented by the symbol (*WV*) (see Table 1). To create a periodic, linear surface wave at a mesh boundary. George Biddell Airy26's linear wave theory serves as the foundation for the model. It is assumed that this linear wave enters the computational domain from a reservoir with a flat bottom. A linear wave is characterized by wave number ($k=2\pi/\lambda$), wave frequency (ω), the wavelength (λ), and wave amplitude (A). The coordinate in the vertical direction of the wave's free surface height, represented as $z = \eta(x,t)$, describes the wave.

$$\eta = A \cos (kx - \omega t + \varphi) \qquad (2.9)$$

The amplitude of the wave (A) is smaller than the depth of water (h), where φ represents the phase shift angle. The wave speed $c = \omega/k$ is expressed as:

$$c^2 = \frac{g\lambda}{2\pi} tanh\, \frac{2\pi h}{\lambda} \qquad (2.10)$$

A 2-meter-wide outflow boundary designated for wave absorption or wave softening is called the downstream. The symbol (*W*) designates a wall as the bottom boundary condition. The no-slip and no-penetration wall boundary conditions, as employed by Trivedi et al. (2023)[34], are applied. The sides of the channel are defined as symmetry (*S*). Therefore, it is expected that the intended physical geometry, flow pattern, and thermal solution will exhibit symmetrical characteristics. The upper boundary condition designates a free surface with 0.5 fluid fraction and a stagnation pressure (*P*) of 101325 Pascal in order to take air-water interactions into account.

Three different types of probes are used to collect the data for this simulation: airflow meters, pressure gauges, and free surface/wave probes (see Fig. 2). In order to measure and track free surface or wave height, wave probes are placed strategically in the center of the OWC chamber, in front of the model test, and at the input of the wave generator. In order to study pressure distribution and system changes, pressure probe that are located on the OWC chamber and the turbine duct provide vital information on differential pressure. An airflow gauge is located at the turbine orifice center, aimed at measuring and assessing airflow behavior, along with incoming and outgoing airflow velocity in the OWC system.

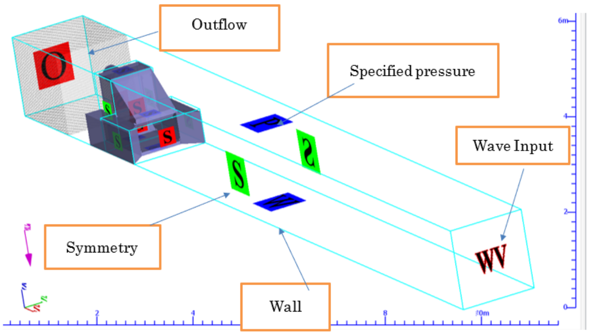

Fig 1. Boundary Conditions.

Table 1 Conditions for numerical testing

Parameter	Variables
Wave Generation (Test scenario)	H (m) and T (s)
	H (m) = 0.125**; 0.1875; 0.25
	T (s) = 1.77; 2.12; 2.47**
Water conditions	Tides = *HWL*; *MSL**; *LWL*
Installation conditions	Water depth = *D085*; *D075**; *D065*

* *MSL* is equivalent to *D075* (see Fig. 3)

** Certain scenarios are made into fixed variables

Wave height and wave period variants totaling three wave height variations and three wave period variations are included in the numerical testing. Additionally, variations are added based on water conditions influenced by tides, namely High Water Level (*HWL* = 0.85 m), Mean Sea Level (*MSL* = 0.75 m), and Low Water Level (*LWL* = 0.65 m). The depth of the L-OWC device during installation is also varied with depth variations (D), namely D = 0.85 m (*D085*), D = 0.75 m (*D075*), and D = 0.65 m (*D065*), as outlined in Table 1 and see Fig. 2. The simulated wave variations represent characteristics of waves with relatively short wave periods. Regular waves are employed in this simulation to facilitate the observation of the wave behavior entering the OWC chamber. The design involves an L-OWC with a turbine diameter scenario of 0.2 meters. The testing scale has been set to 1:8, which corresponds to the scale used in the experimental validation.

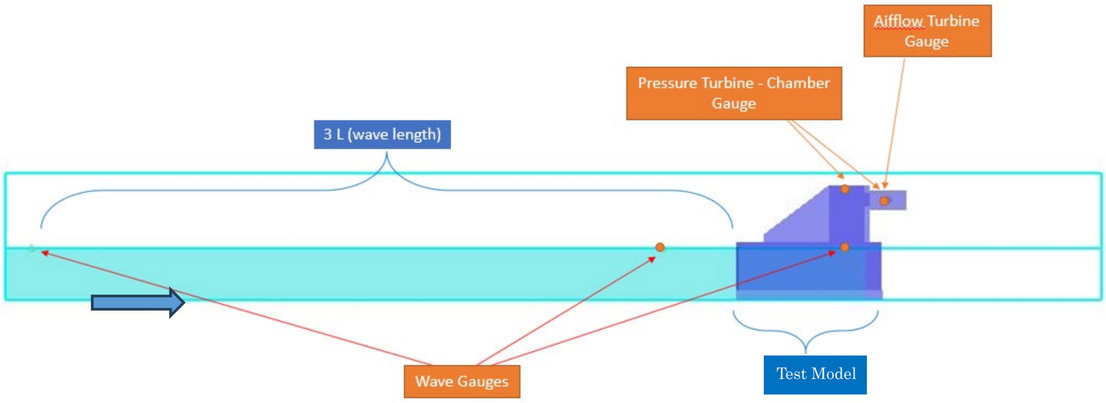

Fig. 2: Numerical set-ups.

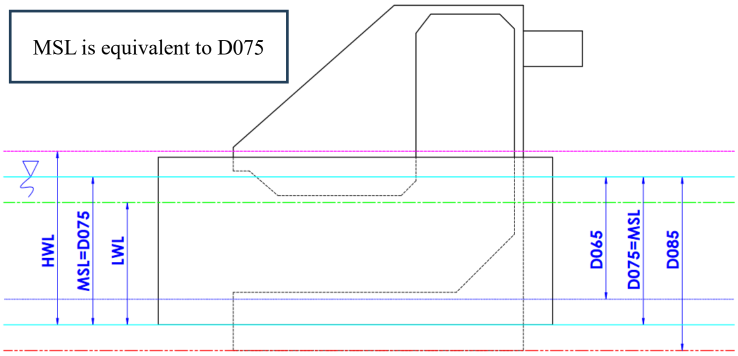

Fig. 3: Variations in water conditions: tides (*HWL*; *MSL*; *LWL*) and installation of L-OWC devices (*D085*; *D075*; *D065*)

2.3 Test model

The L-OWC chamber that has been successfully commissioned by WSE Australia serves as the experimental model design for the research that was conducted (see Fig 4 A)[35]. The OWC design in Fig. 4 (A) and (B) is also equipped with a pontoon as a carrier as well as directing and capturing wave energy entering the chamber.

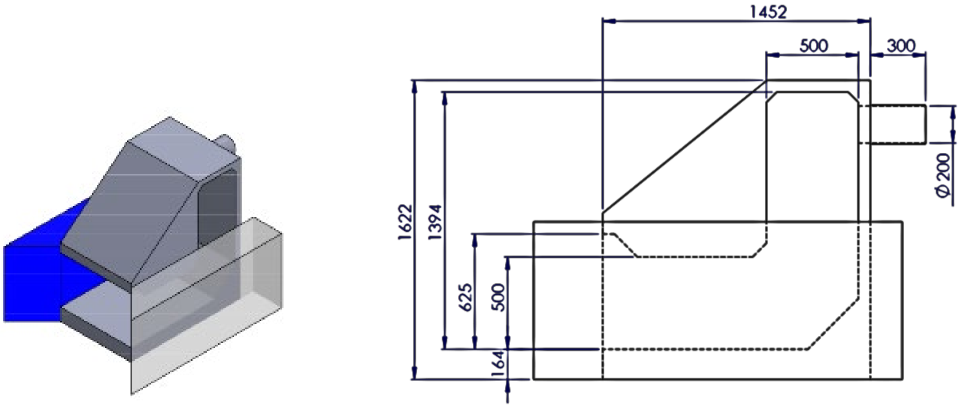

Fig. 4: The OWC L-shaped chamber test model.

2.4 Dimensional analysis

Power of wave energy is the amount of energy produced per meter of approaching ocean waves. that are directed toward the wave energy converter (WEC) equipment. Thus, in a broad context, The power of waves flowing in from the ocean wave is stated as follows[36]:

$$P = \frac{\rho g^2}{64\pi} H_{m0}^2 T_e \approx \left(0.5 \frac{kW}{m^2 s}\right) H_{m0}^2 T_e \qquad (2.11)$$

A few essential factors typically characterize the wave spectrum, and the majority of these are determined using spectral moments, which are defined as follows.:

$$P_{wave\ front} = \frac{P_{water}.g.h^2.\lambda}{16\,T} + \frac{1+4\,\pi\,d\,/\,\lambda}{sinh\,(4\,\pi\,d/\lambda)} \qquad (2.12)$$

Both the air differential pressure rate and the entering airflow velocity into the turbine have an impact on the power input within the duct of an OWC-type wave energy turbine.The power (P_{in}) is expressed as follows[37]:

$$P_{in} = \left(dP + \rho\frac{v^2}{2}\right) A.v_{air} \qquad (2.13)$$

$$P_{in\ airflow} = \frac{1}{2}\,\rho.A.v_{air}{}^3 \qquad (2.14)$$

$$P_{in\ dP} = dP.A.v_{air} \qquad (2.15)$$

The OWC Wave Power Plant's energy source is the turbine, as indicated by equations 2.14 and 2.15. By utilizing the energy of dP and v, the turbine generates electricity.

3. Result and Discussion

3.1 Validation

The validation was conducted by comparing the experiments results with numerical simulation. A mesh independence study was performed to ensure that the selected total mesh size had reached optimal results, as shown in Fig. 5.

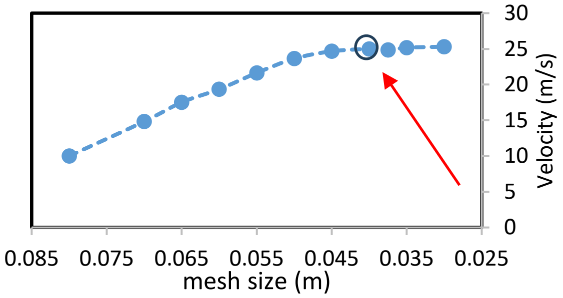

Fig. 5: Mesh Independence Study

The grid resolution method uses past understanding of the problem's physics to calculate the mesh size. The mesh size is incrementally increased until no significant improvement in performance is observed with further mesh refinement[38]. In this study, a mesh independence study was conducted, as depicted in Fig. 5, with the graph indicating the appropriate mesh size for this simulation, which is smaller than 0.045 m. For this simulation work, a mesh size of 0.04 m was employed, meeting the criteria established in the mesh independence study. Grid-independent numerical solutions are a key requirement in the verification and validation process, typically achieved through extrapolation methods[39].

Utilizing pressure data inside the L-shaped chamber and wave measurement data in the chamber area is necessary for the validation of numerical and experimental data. The validation findings, having a 0.07 Root Mean Square Error (RMSE), show the agreement between wave heights in the chamber region in Fig. 6 (A). There are differences between the data from the experiment and the numerical simulation because in the experiment, a mechanical ramp-up of 10s is required before the input waves form according to the testing scenario (see the green rectangular in Fig. 6 (A)). In the CFD, the input waves match the testing scenario.

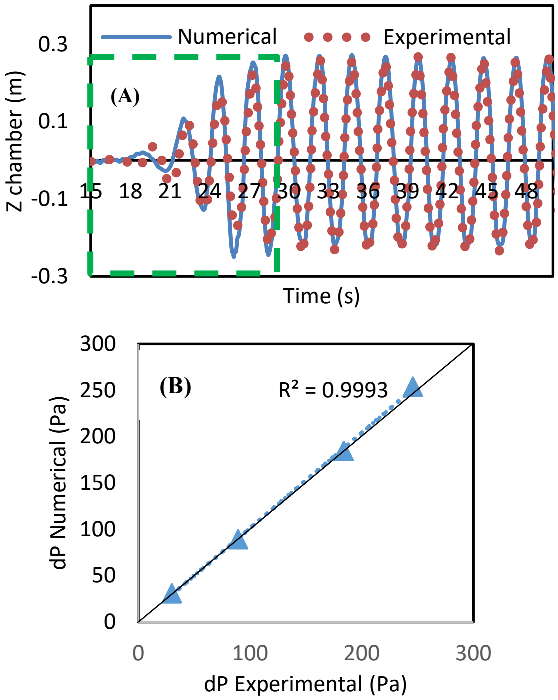

Fig. 6: (A) The results of comparing the experimental and numerical air differential pressure, (B) The comparison of time-series wave height isolation in an experimental and a numerical.

Furthermore, to attain comprehensive validation results beyond wave height isolation within the chamber, a comparison was conducted between numerical pressure difference outcomes and experimental findings. The coefficient of determination, also known as R-squared (R2), in Fig. 6 (B) shows how the numerical and experimental results for differential pressure compare. For the comparison of pressure differences, the R2 value is 0.9993. This result demonstrates how consistent and dependable the numerical simulation is when compared to experimental findings.

3.2 Contour, vector, streamline visualization in L-OWC

The vector of air flow velocity and contour of water flow velocity entering the L-OWC column are shown in Fig. 7. Figures 7 (A) and (B) depict the process of the entry of a mass or volume of water with a specific velocity into the L-OWC chamber. The entry of the mass or volume of water into the chamber results in pneumatic pressure, generating an increased air flow velocity out of the chamber towards the turbine duct. Conversely, the reverse process is illustrated in Fig. 7 (C) and (D), resulting in bidirectional airflow.

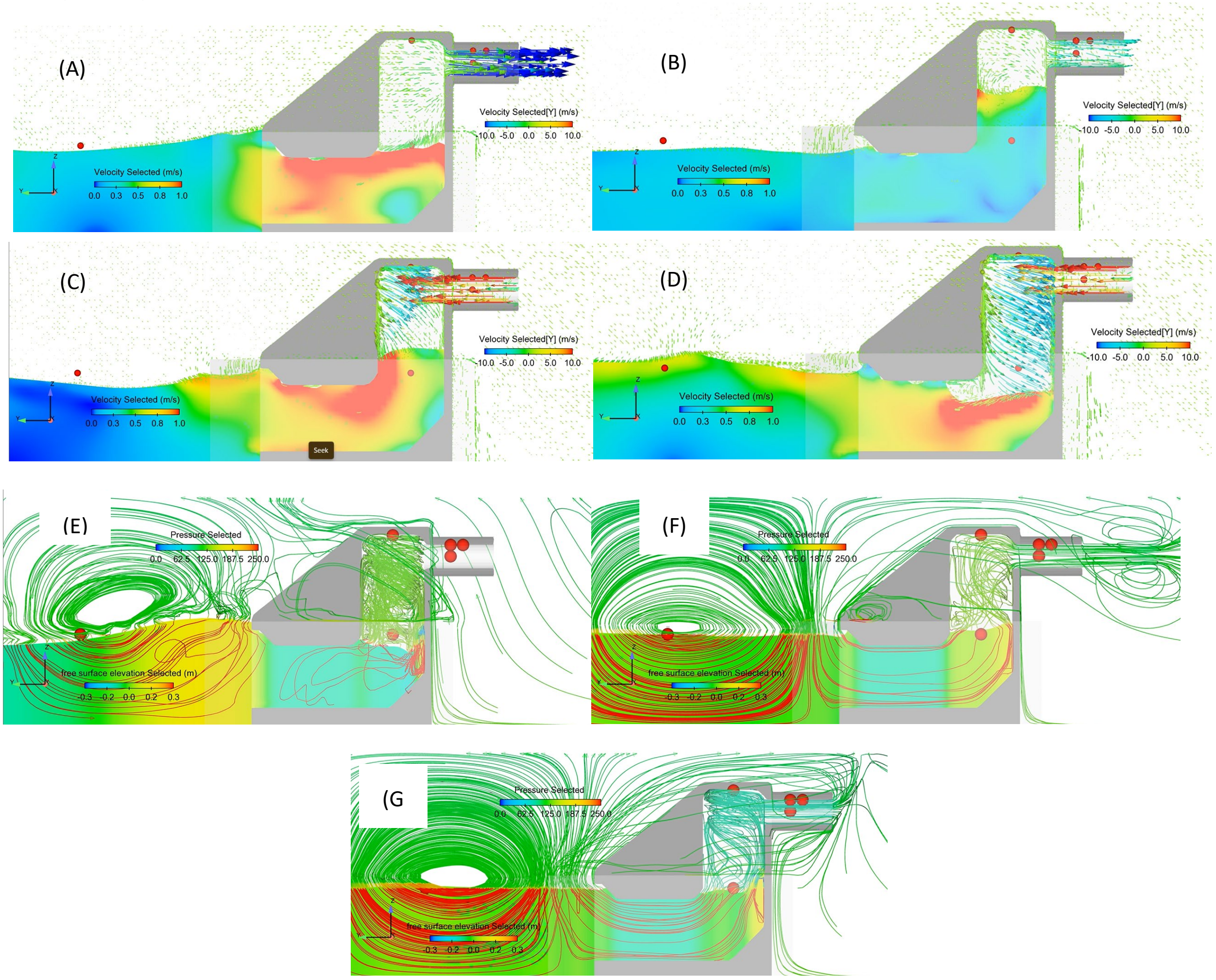

Fig 7: The vector of air flow velocity and contour of water velocity at H = 0.25 m; T = 2.47s (A-D), The streamline with color-coded pressure lines and contour lines of water elevation at H = 0.125 m; T = 1.77s (E-G), in the MSL scenario.

In image 7 A-D, the test scenario H25 T247 demonstrates optimal water flow speed entering the L-OWC chamber, resulting in water oscillation inside the chamber. Meanwhile, in image 7 E-D, under the scenario H125 T177, it is indicated that the contour of elevation and water flow does not optimally enter the chamber and is even reflected out of the chamber. This is depicted by the rotating streamline pattern in front of the L-OWC door and suboptimal elevation contour showing oscillations. In L-OWC chamber shown in image 7 (E), there is a vortex occurring in the L-OWC chamber, and the in-and-out flow velocity in the chamber does not exhibit high values.

3.3 Influence $Z_{chamber}$ and V_{air}

On Figure 8, it illustrates a correlation between wave oscillation inside the L-OWC chamber ($Z_{chamber}$) and the airflow velocity in the turbine duct (V_{air}), which increases with the increasing input wave period (T) at the same input wave height (H = 0.125 m). Variations in tidal levels (*HWL*, *MSL*, and *LWL*) and the water depth of the L-OWC device affect $Z_{chamber}$ in the chamber and V_{air} in the turbine duct. In the test scenario with various T on Fig. 8, it shows that the highest water oscillation and airflow velocity occur in the *HWL* scenario with a variation in period T = 2.47 s, with $Z_{chamber}$ of 0.65 m and V_{air} of 12.8 m/s. The lowest water oscillation and airflow velocity are in the *HWL* scenario with T = 1.77 s, with $Z_{chamber}$ of 0.158 m and V_{air} of 4.75 m/s. The depth of water in the L-OWC device installation does not significantly affect it compared to the influence of tidal levels.

The correlation between variations in wave height (H) at the same period, namely T = 2.47 s, in the airflow velocity in the turbine duct (V_{air}) and the oscillation within the chamber ($Z_{chamber}$) is depicted in Fig. 9. Increased variations in H correspond to the increased $Z_{chamber}$ and V_{air} within the L-OWC chamber. In Figure 9, variations in tidal conditions (*HWL*, *MSL*, and *LWL*) and water depth in the L-OWC device affect $Z_{chamber}$ and V_{air}. In each wave generation test scenario, the *LWL* condition represents the condition with the lowest $Z_{chamber}$, and V_{air} has the lowest values. The highest water oscillation ($Z_{chamber}$) is found in all *HWL* scenarios, with the highest $\text{Z-}_{\text{hamber}}$ value being 0.87 m, and the highest V_{air} is found in the Depth condition of 0.80m (*D085*), which is 21.2 m/s.

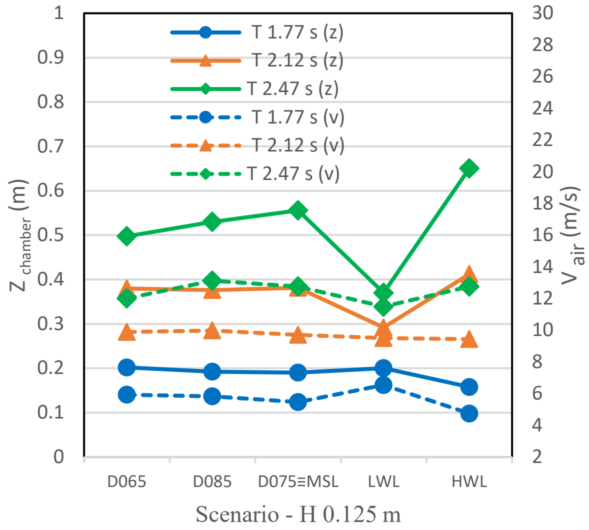

Fig. 8: The influence of various T with H = 0.125 m on water oscillation ($Z_{chamber}$) and airflow velocity (V_{air})

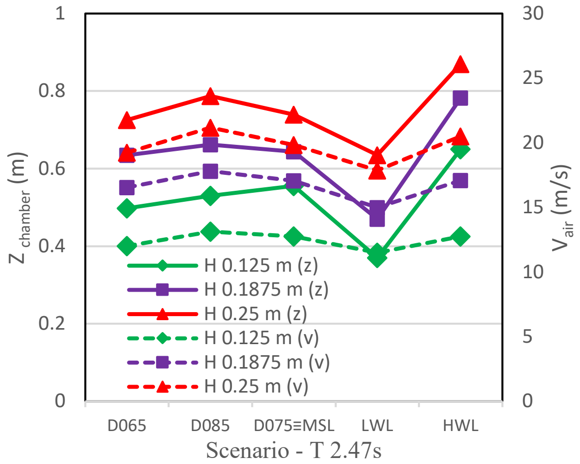

Fig. 9: The influence of various H with T = 2.47 s on water oscillation ($Z_{chamber}$) and airflow velocity (V_{air})

3.4 Influence $Z_{chamber}$ and Differential Pressure (dP)

In Figure 10, it is illustrated that the influence of variations in the wave input period (T) at the same wave height (H = 0.125 m) has an effect on $Z_{chamber}$ and dP. As the Input Period (H) increases, $Z_{chamber}$ and dP in the L-OWC chamber also increase. The highest values for $Z_{chamber}$ and dP are found in the T = 2.47 s test scenario, with $Z_{chamber}$ = 0.65 m in the *HWL* scenario and dP = 99.6 pascal in the *D085* scenario. The lowest values for $Z_{chamber}$ and dP are found at T = 1.77 s with values of 0.16 m and 8.6 pascal, respectively. Variations in tidal conditions (*HWL*, *MSL*, and *LWL*) and water depth in the L-OWC device affect $\text{Z-}_{\text{chamber}}$ in the chamber and diiferential pressure (dP) in the turbine duct. The influence of water depth conditions does not significantly affect $Z_{chamber}$ and dP. Significant effects are shown by the influence of water depth installation for the L-OWC device with input periods longer than T = 2.47 s.

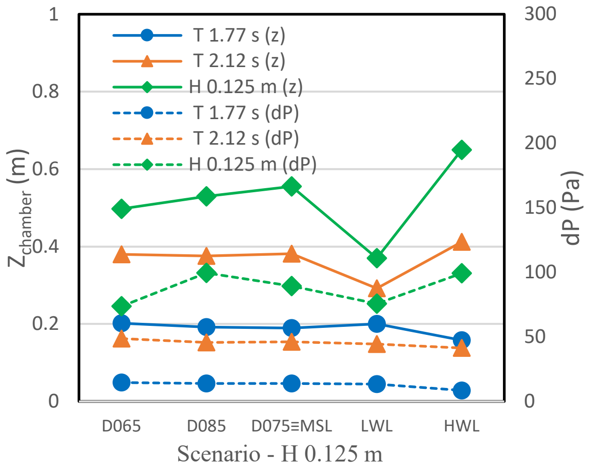

Fig. 10: The influence of various T with H = 0.125 m on water oscillation ($Z_{chamber}$) in the chamber and diiferential pressure (dP)

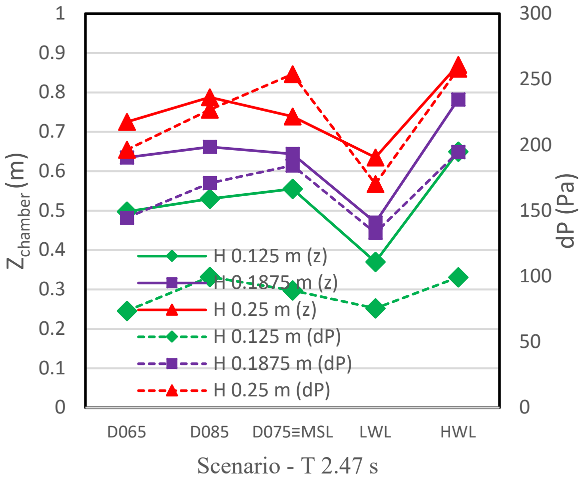

Fig. 11: The influence of various H with T = 2.47s on water oscillation ($Z_{chamber}$) and diiferential pressure (dP).

The influence of variations in Wave Height (H) at the same wave input period (T = 2.47 s) is shown in Fig. 11. The increase in the variation of wave height (H) causes water mass to enter the L-OWC chamber, affecting $Z_{chamber}$ and dP in the L-OWC chamber. In Figure 11, $Z_{chamber}$ and dP are highest at H = 0.25 m and lowest at H = 0.125 m. The values of $Z_{chamber}$ and dP are highest in the *HWL* scenario, reaching 0.87 m and 257.9 pascal, respectively. The *LWL* scenario and DO65 scenario respectively do not provide optimal results in increasing $Z_{chamber}$ or dP in the chamber and turbine duct.. Meanwhile, the optimal average values are found in *D075* or *MSL* scenarios.

3.5. L-OWC performance in all conditions and scenarios

The correlation of various test scenarios on water conditions and L-OWC device installation conditions, specifically regarding water conditions and installation depth variations, is illustrated in Fig. 12; (A), (B), and (C), respectively. The test results indicate that the H125 T177 scenario shows the lowest and suboptimal results in all variations of water conditions and L-OWC device installation. On the other hand, the H25 T247 scenario proves to be the best and optimal in all tested conditions. Figure 12 highlights the variation in water conditions, particularly the low water level (*LWL*), as a crucial consideration due to its significant influence on differential pressure and airflow velocity, subsequently affecting the performance of the L-OWC device. The significant decline in the performance of the L-OWC design during Low Water Level (LWL) conditions should be considered when planning the installation of L-OWC in deeper seawater or avoiding installation in areas with a high tidal range.

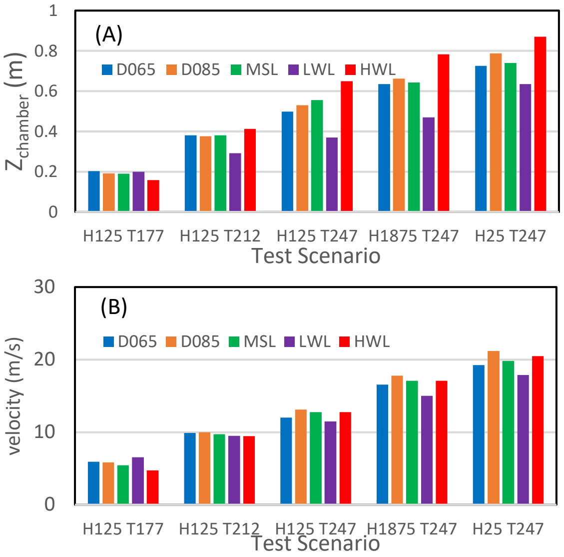

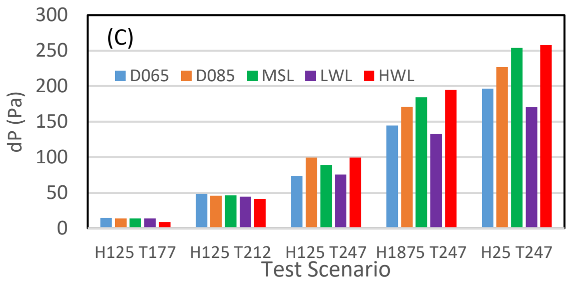

Fig. 12: Test scenarios for water conditions (tides) and L-OWC device installation conditions on; (A) $Z_{chamber}$,(B) velocity, (C) Differential pressure

3.6 Power performance L-OWC

The power generated by the L-OWC is influenced by several factors that have been discussed, including wave height and period characteristics, tidal conditions, and the water depth at which the device is installed. The compatibility between the L-OWC device and the waters or wave characteristics will result in optimal power output. In Figure 13, it is illustrated that airflow velocity (V_{air}) and differential pressure (dP), as shown in Fig.12, correlate significantly with power, as expressed in the equation 2.15. The power output is most optimal in the H25 T247 wave generation scenario compared to other test scenarios. This indicates that the L-OWC device performs well at longer wave periods (T = 2.47 s).

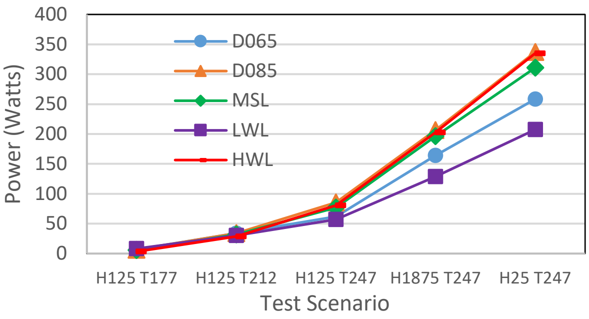

Fig. 13 : Power L-OWC in all test scenarios and conditions.

The L-OWC device also demonstrates the best performance under rising tide conditions (*HWL*) with a power of 355 Watts and with the device installed at the deepest water depth, namely *D085* with a power of up to 357 Watts. In Figure 13, it is shown that under ebb tide conditions (*LWL*) and with the device installed at a depth that does not meet certain criteria (illustrated as *D065*), the performance will decrease. Therefore, it is necessary to ensure that the device is always submerged in water under adequate conditions for oscillation.

4. Conclusions

The study's findings indicate that the wave dynamics entering the chamber significantly impact L-OWC performance. Optimal scenarios show effective water entry, enhancing chamber oscillation, airflow, and differential pressure within the chamber and turbine duct. Suboptimal conditions, where waves reflect and cannot be fully captured by the L-OWC chamber.

Optimal performance of L-OWC correlates with higher wave heights, relatively longer wave periods, and High Water Level (HWL) conditions, resulting in increased water oscillation (Zchamber), airflow velocity (Vair) and differential pressure (dP). Tidal variations exert significant influence, whereas water depth shows minimal impact compared to tidal effects. These findings underscore the importance of wave characteristics and tidal conditions in optimizing efficiency and design of L-OWC for effective wave energy conversion.

Several test scenario conditions with D = 0.85 m resulted in better water surface oscillation, differential pressure, and air flow velocity compared to other installation water depth conditions.The correlation of tidal conditions with wave generation test scenarios shows results that need significant attention. LWL conditions experience a decrease in system performance, as indicated by the decrease in differential pressure, and air flow velocity in the L-OWC chamber and turbine duct. In HWL conditions, the system operates well, with a high air flow velocity of 21.2 m/s and a differential pressure of 257.9 pascal in the test scenario H = 0.25 m; T = 2.47 s.

The airflow velocity (V_{air}) and differential pressure (dP) significantly correlate with power output. The L-OWC device performs best at longer wave periods (T = 2.47 s) and under rising tide conditions (HWL) with power output up to 357 Watts when installed at the deepest water depth (D085). Conversely, performance decreases under ebb tide conditions (LWL) and at inadequate depths (D065). Thus, for optimal efficiency, the device must be submerged under suitable conditions for oscillation. The L-OWC device is recommended for installation in areas with low tidal variations or as per the study's recommendation for the floating type L-OWC, which is not affected by tidal variations. The recommendation for future research is to test the L-OWC design with a wider range of wave periods and heights scenarios.

Acknowledgements

The House Program of New and Renewable Energy, Research Organization for Energy and Manufacture, BRIN, Indonesia, funded the experimental endeavors with grant number 13/III.3/HK/2022.

Nomenclature

$Z_{chamber}$	water level oscillations in the chamber (m)
P	input power of the OWC (W)
V_{air}	airflow velocity in the turbine duct (m/s)
dP	differential pressure between chamber and turbine duct (pascal)
A	cross-sectional area of the turbine duct (square meters)
H	wave height input (m)
T	wave period input (s)
Greek symbols	
μ	dynamic viscosity
∇^2	vector Laplacian
f_m	volume fraction
λ	wavelength
ω	wave frequency

References

1) A.F.O. Falcão, and J.C.C. Henriques, "Oscillating-water-column wave energy converters and air turbines: a review," *Renew. Energy*, **85** (*January*) 1391–1424 (2016). doi:10.1016/j.renene.2015.07.086.
2) R. Adiputra, M.I. Habib, Erwandi, A.R. Prabowo, A.S.D. Marta, W.W. Pandoe, N. Puryantini, R.B. Sitanggang, and A. Nurfanani, "Ocean Renewable Energy in Indonesia : A Brief on the Current State and Development Potential," 2023. doi:10.55981/brin.900.c782.
3) A. Terrero González, P. Dunning, I. Howard, K. McKee, and M. Wiercigroch, "Is wave energy untapped potential?," *Int. J. Mech. Sci.*, **205** (*February*) (2021). doi:10.1016/j.ijmecsci.2021.106544.
4) A.A. Medina Rodríguez, G. Posada Vanegas, B.E. Vega Serratos, I. Oderiz Martinez, E. Mendoza, J.M. Blanco Ilzarbe, V. Sundar, and R. Silva, "The hydrodynamic performance of a shore-based oscillating water column device under random wave conditions," *Ocean Eng.*, **269** (*August 2022*) 113573 (2023). doi:10.1016/j.oceaneng.2022.113573.
5) N. Ansarifard, A. Fleming, A. Henderson, S.S. Kianejad, S. Chai, and J. Orphin, "Comparison of inflow and outflow radial air turbines in vented and bidirectional owc wave energy converters," *Energy*, **182** 159–176 (2019). doi:10.1016/j.energy.2019.06.041.
6) I. López, R. Carballo, D.M. Fouz, and G. Iglesias, "Design selection and geometry in owc wave energy converters for performance," *Energies*, **14** (*6*) 1–18 (2021). doi:10.3390/en14061707.
7) Y. Cui, Z. Liu, X. Zhang, and C. Xu, "Review of cfd studies on axial-flow self-rectifying turbines for owc wave energy conversion," *Ocean Eng.*, **175** (*December 2018*) 80–102 (2019). doi:10.1016/j.oceaneng.2019.01.040.
8) P. Boccotti, "Comparison between a u-owc and a conventional owc," *Ocean Eng.*, **34** (*5–6*) 799–805 (2007). doi:10.1016/j.oceaneng.2006.04.005.
9) K. Rezanejad, J. Bhattacharjee, and C. Guedes Soares, "Stepped sea bottom effects on the efficiency of nearshore oscillating water column device," *Ocean*

Eng., **70** 25–38 (2013). doi:10.1016/j.oceaneng.2013.05.029.

10) K. Rezanejad, C. Guedes Soares, I. López, and R. Carballo, "Experimental and numerical investigation of the hydrodynamic performance of an oscillating water column wave energy converter," *Renew. Energy*, **106** 1–16 (2017). doi:10.1016/j.renene.2017.01.003.
11) M.M. Samak, H. Elgamal, and A.M. Nagib Elmekawy, "The contribution of l-shaped front wall in the improvement of the oscillating water column wave energy converter performance," *Energy*, **226** 120421 (2021). doi:10.1016/j.energy.2021.120421.
12) R.P.F. Gomes, J.C.C. Henriques, L.M.C. Gato, and A.F.O. Falcão, "Hydrodynamic optimization of an axisymmetric floating oscillating water column for wave energy conversion," *Renew. Energy*, **44** 328–339 (2012). doi:10.1016/j.renene.2012.01.105.
13) Y. Luo, Z. Wang, G. Peng, Y. Xiao, L. Zhai, X. Liu, and Q. Zhang, "Numerical simulation of a heave-only floating owc (oscillating water column) device," *Energy*, **76** 799–806 (2014). doi:10.1016/j.energy.2014.08.079.
14) B. Pereiras, F. Castro, A. el Marjani, and M.A. Rodríguez, "An improved radial impulse turbine for owc," *Renew. Energy*, **36** (*5*) 1477–1484 (2011). doi:10.1016/j.renene.2010.10.013.
15) A. Thakker, F. Hourigan, T.S. Dhanasekaran, M. El Hemry, Z. Usmani, and J. Ryan, "Design and performance analysis of impulse turbine for a wave energy power plant," *Int. J. Energy Res.*, **29** (*1*) 13–36 (2005). doi:10.1002/er.1034.
16) B.S. Lopes, L.M.C. Gato, A.F.O. Falcão, and J.C.C. Henriques, "Test results of a novel twin-rotor radial inflow self-rectifying air turbine for owc wave energy converters," *Energy*, **170** 869–879 (2019). doi:10.1016/j.energy.2018.12.078.
17) B. Bouali, and S. Larbi, "Contribution to the geometry optimization of an oscillating water column wave energy converter," *Energy Procedia*, **36** 565–573 (2013). doi:10.1016/j.egypro.2013.07.065.
18) N. Dizadji, and S.E. Sajadian, "Modeling and optimization of the chamber of owc system," *Energy*, **36** (*5*) 2360–2366 (2011). doi:10.1016/j.energy.2011.01.010.
19) A.S.D. Marta, Deendarlianto, W. Kongko, Indarto, Fauzun, and A.T. Rohman, "The influence of wave height and period on airflow velocity and differential pressure in l-shaped oscillating water column (l-owc) chamber for wave energy converter (wec)," *Asia-Pacific J. Sci. Technol.*, **In Press** (*2024*) 14 (2024).
20) J. Hayward, "Wave energy cost projections a report for wave swell energy limited," *CSIRO Energy Citation, Aust. Natl. Sci. Agency Wave*, (*October*) (2021).
21) K. Rezanejad, J.F.M. Gadelho, and C. Guedes Soares, "Hydrodynamic analysis of an oscillating water column wave energy converter in the stepped bottom condition using cfd," *Renew. Energy*, **135** 1241–1259 (2019). doi:10.1016/j.renene.2018.09.034.
22) K. Rezanejad, A. Souto-Iglesias, and C. Guedes Soares, "Experimental investigation on the hydrodynamic performance of an l-shaped duct oscillating water column wave energy converter," *Ocean Eng.*, **173** (*November 2017*) 388–398 (2019). doi:10.1016/j.oceaneng.2019.01.009.
23) Y.S. Kuo, C.Y. Chung, S.C. Hsiao, and Y.K. Wang, "Hydrodynamic characteristics of oscillating water column caisson breakwaters," *Renew. Energy*, **103** 439–447 (2017). doi:10.1016/j.renene.2016.11.028.
24) Z. Liu, C. Xu, K. Kim, J. Choi, and B. soo Hyun, "An integrated numerical model for the chamber-turbine system of an oscillating water column wave energy converter," *Renew. Sustain. Energy Rev.*, **149** (*April*) 111350 (2021). doi:10.1016/j.rser.2021.111350.
25) V. Yakhot, and S.A. Orszag, "Renormalization group analysis of turbulence. i. basic theory," *J. Sci. Comput.*, **1** (*1*) 3–51 (1986). doi:10.1007/BF01061452.
26) H.L. Wu, S.C. Hsiao, and T.C. Lin, "Evolution of a two-layer fluid for solitary waves propagating over a submarine trench," *Ocean Eng.*, **110** 36–50 (2015). doi:10.1016/j.oceaneng.2015.10.004.
27) T. Vyzikas, S. Deshoulières, O. Giroux, M. Barton, and D. Greaves, "Numerical study of fixed oscillating water column with rans-type two-phase cfd model," *Renew. Energy*, **102** 294–305 (2017). doi:10.1016/j.renene.2016.10.044.
28) Z. Liu, B.S. Hyun, and K. Hong, "Numerical study of air chamber for oscillating water column wave energy convertor," *China Ocean Eng.*, **25** (*1*) 169–178 (2011). doi:10.1007/s13344-011-0015-8.
29) C.W. Hirt and B. D. Nichols, "Chaotic self-tuning pid controller based on fuzzy wavelet neural network model," *J. Comput. Phys.*, **39** 201–225 (19981). doi:10.1007/s40998-018-0069-1.
30) B. van Leer, "Towards the ultimate conservative difference scheme. v. a second-order sequel to godunov's method," *J. Comput. Phys.*, **32** (*1*) 101–136 (1979). doi:10.1016/0021-9991(79)90145-1.
31) Flow Science, "Flow-3d user manual version 9.3," (*1*) 1–739 (2008). www.flow3d.com.
32) M. Qu, D. Yu, Z. Xu, and Z. Gao, "The effect of the elliptical front wall on energy conversion performance of the offshore owc chamber: a numerical study," *Energy*, **255** 124428 (2022). doi:10.1016/j.energy.2022.124428.
33) G. Wolters, M. Van Gent, W. Allsop, L. Hamm, and D. Mühlestein, "HYDRALAB iii: guidelines for physical model testing of rubble mound breakwaters," *Coasts, Mar. Struct. Break. Adapt. to Chang. - Proc. 9th Int. Conf.*, **2** (*December 2013*) 659–670 (2010). doi:10.1680/cmsb.41318.0062.

34) K. Trivedi, A.R. Ray, P.A. Krishnan, S. Koley, and T. Sahoo, “Hydrodynamics of an owc device in irregular incident waves using rans model,” *Fluids*, **8** (*1*) 1–31 (2023). doi:10.3390/fluids8010027.
35) D. Brown, and Justin, “UniWave200 King Island Development Application,” 2019.
36) S.K. Mishra, B. Appasani, A.V. Jha, I. Garrido, and A.J. Garrido, “Centralized airflow control to reduce output power variation in a complex owc ocean energy network,” *Complexity*, **2020** (2020). doi:10.1155/2020/2625301.
37) S. Mishra, S. Purwar, and N. Kishor, “Maximizing output power in oscillating water column wave power plants: an optimization based mppt algorithm,” *Technologies*, **6** (*1*) 15 (2018). doi:10.3390/technologies6010015.
38) K.M. Almohammadi, D.B. Ingham, L. Ma, and M. Pourkashan, “Computational fluid dynamics (cfd) mesh independency techniques for a straight blade vertical axis wind turbine,” *Energy*, **58** 483–493 (2013). doi:10.1016/j.energy.2013.06.012.
39) A. Seeni, P. Rajendran, and H. Mamat, “A cfd mesh independent solution technique for low reynolds number propeller,” *CFD Lett.*, **11** (*10*) 15–30 (2019).